

Inkjet-Printed Microlenses Integrated onto Organic Photodiodes for Highly Accurate Proximity Sensing

Mervin Seiberlich, Qiaoshuang Zhang, Ali Veysel Tunc, Kai Xia, Luis Arturo Ruiz-Preciado, Stefan Schliske, Konstantinos Falis, Noah Strobel, Uli Lemmer, and Gerardo Hernandez-Sosa*

The current needs for optical detectors in industrial and consumer electronics require sensors with thin form-factors, high performance and a facile fabrication and integration. In this work, the integration of inkjet printed microlenses onto solution-processed organic photodiodes is demonstrated to enable high-accuracy proximity sensing via the focused induced photoresponse (FIP) effect. By precisely controlling the ink deposition and substrate properties, it is able to tune the microlens focal length from 150 to 775 μm . This allows to the appropriate microlens design to be chosen to take advantage of the FIP effect. By comparing the photocurrent ration of a device with and without microlenses, absolute proximity measurements in the range of 100 μm to 4 mm are achieved. Champion devices yield an accuracy of down to $\pm 50 \mu\text{m}$ within three standard deviations (3σ). These results highlight the potential of the microlens-OPD integration for highly accurate and close-distance proximity applications in a variety of fields.

signal- or imaging systems.^[1–3] This versatility of use-cases explains the success-story of optical sensing as a key-technology in current industrial and consumer electronics. However, with the fast development of new fields such as robotics, hybrid, and flexible electronics or wearable devices and their need for miniaturization, sensors entailing thin form-factors, high performance, and facile fabrication and integration are urgently required. The emerging research in printed and flexible optoelectronics promises addressing these needs while opening complementary opportunities where classical silicon technology is limited due to its rigid nature and limited raw materials. The main advantages of printed electronics

1. Introduction

The complex nature of light and its interplay with matter open tremendous possibilities for optical sensors, with applications in areas like environmental monitoring, medical diagnostics, and

technology combine a freedom of design through precise ink deposition, ultrathin form factors, the possibility of using flexible substrates and the versatility of carbon-based semiconductors with a wide-range of optoelectronic properties.^[4] Among these technologies, printed organic photodiodes (OPDs) have been used to fabricate flexible pulse-oxyimeters,^[5,6] color-selective systems for visible light communication^[7] or an all-polymer integrated twilight switch^[8] to cite some examples. Recent research efforts have also led to devices showing a broad-band absorption,^[9,10] noise reduction,^[11,12] color- and polarization-selectivity,^[7,13–16] and detection speeds in the MHz regime.^[17]

M. Seiberlich, Q. Zhang, A. V. Tunc, K. Xia, L. A. Ruiz-Preciado, S. Schliske, K. Falis, N. Strobel, U. Lemmer, G. Hernandez-Sosa
 Light Technology Institute
 Karlsruhe Institute of Technology
 Engesserstr. 13, 76131 Karlsruhe, Germany
 E-mail: gerardo.sosa@kit.edu

M. Seiberlich, A. V. Tunc, K. Xia, L. A. Ruiz-Preciado, S. Schliske, N. Strobel, U. Lemmer, G. Hernandez-Sosa
 InnovationLab
 Speyererstr. 4, 69115 Heidelberg, Germany
 U. Lemmer, G. Hernandez-Sosa
 Institute of Microstructure Technology
 Karlsruhe Institute of Technology
 Hermann-von-Helmholtz-Platz 1, 76344 Eggenstein-Leopoldshafen, Germany

 The ORCID identification number(s) for the author(s) of this article can be found under <https://doi.org/10.1002/adsr.202300004>

© 2023 The Authors. Advanced Sensor Research published by Wiley-VCH GmbH. This is an open access article under the terms of the Creative Commons Attribution License, which permits use, distribution and reproduction in any medium, provided the original work is properly cited.

Moreover, digital printing technologies open new possibilities for customized micro- and nanooptics integrated with optoelectronic devices. For example, optical elements for improved light extraction in printed light-emitting devices^[18] or inkjet printed microlens arrays for optical imaging systems^[19–26] have been recently demonstrated. Only recently, Zhang et al. presented an industrial compatible inkjet printing process with an optimized UV-curable ink achieving low shrinkage, high uniformity, and a high fill factor without surface structuring steps like photolithography.^[19] While applications with printed microlenses like flowmetry at the microscale^[24] or the outcoupling of light on top of optical fibers^[25,26] have been presented in the past, the combination with organic electronics technology is still due.

The integration of OPDs with digitally printed micro-optics in a single process would present advantages for the development of

DOI: 10.1002/adsr.202300004

Table 1. Overview proximity sensors utilizing the FIP.

Material	Range	Max resolution	Realization	Refs.
PbS photoconductor	45–165 cm	0.5 mm	Optical lens	[33]
Amorphous silicon	123–126 cm	2 mm	Optical lens	[34]
BDP-OMe:C ₆₀ (OPD)	0–30 mm	N.A.	Optical lens	[35]
QM1:C60 (NIR OPD)	25–50 mm	N.A.	Optical lens	[35]
Dimeric polymethine dyes (NIR OPD)	0–10 mm	N.A.	Optical lens	[36]
P3HT:IDTBR (NIR OPD)	100 μm –4 mm	50 μm	Inkjet-printed microlens	This work

optical systems with new functionalities. In particular, the combination of the UV-curable ink with concepts for the adjustment of the geometry and digital design of microlenses^[19,20,25] could offer customizable properties, high integration, and accurate positioning optical sensors.

In general, there exist a variety of commonly used optical distance measuring approaches. A straightforward method is to use an LED and photodiode (PD) next to each other and measure the reflected light from a target. This has been realized in commercial silicon sensors as well as in devices from organic materials.^[27,28] Hereby the smallest measurable distance is limited by the space between LED and PD and its typically around 1 mm.^[29] A technical successor of this approach is the integration of the light-source and sensor in a vertical stack which can be realized by using a semitransparent PD. The reported measuring range spans from 1 to 10 mm with a resolution of 1 mm.^[30,31] A disadvantage of these techniques is the high dependence of the intensity and directionality of reflected light on the surface properties of the target. This limits the approach to use cases with calibrated surfaces or relative distance measurements. Another optical distance sensing technique is based on triangulation as demonstrated by Oka et al. using a miniaturized silicon-based micro-optical distance sensor.^[32] This device showed a measurement range of 1 mm and an impressive repeatability uncertainty < 3 μm . Nonetheless, the sensor fabrication is relatively complex and the use of stiff material limits its use case for applications such as flexible and stretchable systems. Similar arguments can be said for time-of-flight measurements. A representative example is the commercial silicon-based micro-LIDAR system used by Markvicka et al. yielding a detection range of 5–200 mm with ± 1 mm resolution.^[27]

A technique that solves many of these challenges is the so-called focus-induced photoresponse (FIP) technique. The FIP effect is based on the universally observed irradiance-dependent responsivity of optical sensors and was introduced by Pekkola et al.^[33] In this technique, two semitransparent photodetectors are positioned one after the other in the optical path of a light source (e.g., from an LED or reflected light from an object) focused by a lens. If one sensor is positioned in the focal point of the lens and the other out of it, the irradiance received by each detector will drastically differ. If at least one of the photodetectors is operated in its nonlinear regime, the ratio between their photocurrent responses will represent a unique signature for each distance to the light source. The FIP technique provides several advantages compared to conventional techniques, since it only requires a single point of view, allows for absolute distance

measurements independently of surface properties and even allows for multiplexing of modulated signals.^[33] The technique has been demonstrated to work with different material classes like amorphous silicon, PbS, CdTe, CIGS, CIS, CZTS, as well as for various organic materials.^[33–36] An overview of FIP based proximity measurement ranges and resolutions is shown in **Table 1**.

In this work, we combine the advantages of OPDs with digitally printed microoptics. To show the potential of this approach, we demonstrate optical proximity sensing based on a modified version of the FIP technique. The inkjet-printed microlenses integrated onto OPD are tailored to focus light into the active layer of the device. In our approach, we compare the photocurrent ratio between an OPD with lenses and a reference without. This ratio yields a unique signature for the absolute distance between the light source and the detector. We demonstrate that the inkjet-printing technique not only provides freedom of design in the xy-directions but also a degree of freedom in the z-direction enabling to design the microlenses with different sizes and thus optimizing their focal point to the substrate and device dimensions. To our knowledge, this is the first attempt to integrate solution-processed OPDs with printed microlenses on a single substrate. The achieved resolution down to 50 μm highlights the potential of our approach for highly accurate and close-distance proximity applications.

2. Results and Discussion

To fabricate the combined microlens-OPD devices, we take advantage of the freedom of design of digital printing not only in the lateral plane but also in the z-direction. By adjusting the number of droplets per lens and adjusting their contact angle by a plasma treatment of the substrate, we are able to tune the geometries and focal length of the lens in the submillimeter range (see **Figure 1a–c**). This ultimately allows us to focus light closer to the absorbing layer of the OPD and could help us in the future to adapt to various substrate thicknesses. A sketch of this principle is shown in **Figure 1d**. The OPDs were deposited on indium tin oxide (ITO) covered glasses and utilized broad-band absorption active layers based on a bulk-heterojunction of P3HT:IDTBR. SnO_x and MoO₃ are used as hole and electron blocking layers, respectively.^[37] The stack was completed by an evaporated Ag top electrode (**Figure 1d**). The pixel size is defined by the overlap of the electrodes yielding and active area of 1 mm².

We investigated the dependence of microlens size when printing from one single droplet to up to 20 droplets per lens. To calculate the effective focal length of the inkjet-printed microlenses,

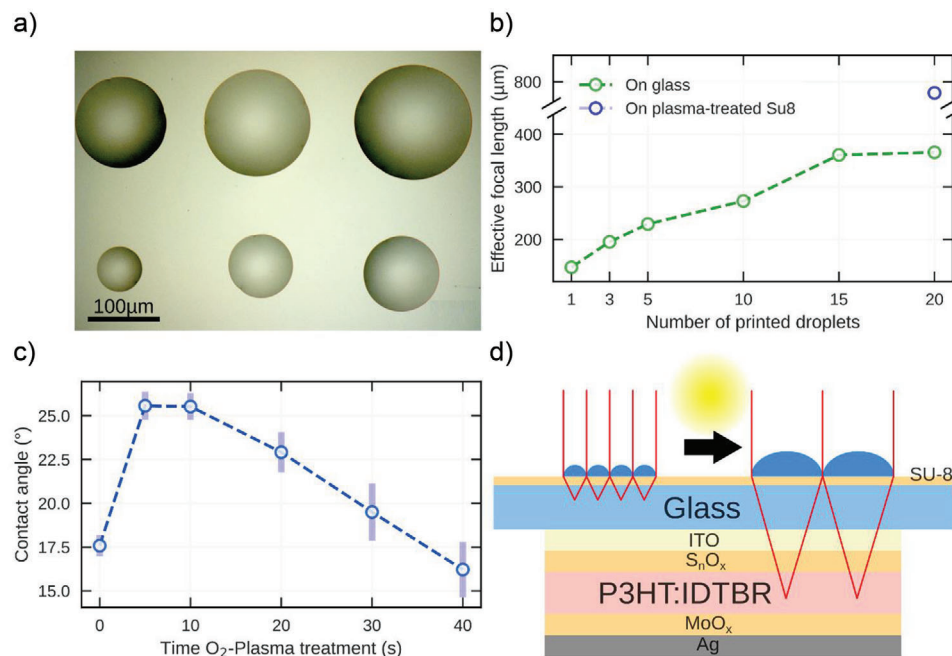


Figure 1. Freedom of design of the focal length: a) Microlenses printed with different numbers of droplets to change their size (scale bar = 100 μm). b) Change in effective focal length of the lenses dependent on the number of droplets and substrate. c) Contact angle of SU-8 ink on SU-8 used for printing the microlens for different O₂-plasma treatment times. Error bars represent 1 σ standard deviation. d) Sketch of inkjet printed microlens on top of an OPD. By adjusting the size and aspect-ratio of the lens, their effective focal length is increased to focus light inside the OPD.

we simulated the optical system comprised of glass substrate and transparent electrode with the commercial ZEMAX optics software. The input parameters are size of the microlens, thickness, and refractive indexes of the layers. As shown in Figure 1a,b, our approach enabled us to change the focal length precisely from 150 to 350 μm . This is comparable to values reported from literature utilizing no extra manufacturing steps such as photolithography.^[20,25] However, due to the thickness of the substrate we needed to tune the focal length further. For this, we introduced an epoxy-based photoresist (SU-8) layer whose surface free energy was modified by O₂-plasma. This layer changes the contact-angle of the printed lens (see Figure 1c) and thus its focal length. Due to the decreased aspect ratio of the lens, we reached a final focal length of 775.4 μm for a microlens with a diameter of 195.4 μm and height 11.7 μm for 20 droplets of 10 pL (Figure 1b). By increasing the diameter of the lens, we also increased their capability of collecting light.

In Figure 2a–f; and Table S1 (Supporting Information), we present the figures of merit (FOM) of the OPDs. All devices show state of the art FOM as well as high reproducibility. At –2 V reverse bias they show low dark current densities j_{Dark} of 20 ± 10 nA cm⁻², high spectral responsivities SR of 310 ± 20 mA W⁻¹, fast speeds 2.2 ± 0.4 MHz, white noise above ≈ 100 Hz (see Figure S2, Supporting Information), a high specific detectivity D^* of $(1.2 \pm 0.5) \times 10^{12}$ Jones and linear dynamic ranges (LDR) of 203 ± 5 dB.

As a measure of the photoresponse for different irradiances, we present in Figure 2e the dynamic range recorded at –2 V bias for the samples with and without microlenses. The LDR is calculated by a 5% deviation to the black dashed line representing a linear dependence of the photoresponse to the illumination power (slope = 1 in log scale). In Figure 2f, the cal-

culated dynamic responsivity is shown. It is an irradiance dependent measure often used in literature to highlight the nonlinear operation regime of the FIP effect. Under high irradiances, the dynamic responsivity shows a measured nonlinear behavior over about two orders of magnitude in favor of the FIP effect. We attribute this drop of the dynamic responsivity with increased irradiance to recombination-losses present in bulk-heterojunctions by the increased density of photogenerated charge carriers, since a high charge density is known to favor bimolecular recombination.^[38–40] In this work, we chose to demonstrate the suitability of this high intensity nonlinear regime to be utilized with the FIP effect. This is different from past approaches working with nonlinearity at lower intensities that can be introduced, e.g., by intentionally fostering nongeminate recombination with an additional extraction barrier in well performing OPDs, as shown by Wang et al. for near-infrared (NIR) OPDs.^[35]

A possible way to enlarge the high intensity nonlinear regime in the future could be to use decreased annealing temperatures that has been shown to have an influence on bimolecular recombination.^[41,42]

We account for the nonlinear behavior by fitting an empirical derived model to the dynamic range (red solid line) similar to the one proposed for PIN PDs by Hong et al.^[43] This enables us to calculate the expected FIP effect on the distance dependent current by simulations. A detailed description of the simulations can be found in Section S2 “Simulation proximity measurements and FIP effect” of the Supporting Information. The blue arrows indicate the total optical power of the fiber-coupled LED used as the light-source for the proximity measurements presented in Figure 3. In the Supporting Information, we present all FOM as a comparison for 0 and –2 V reverse bias (Figures S1–S6,

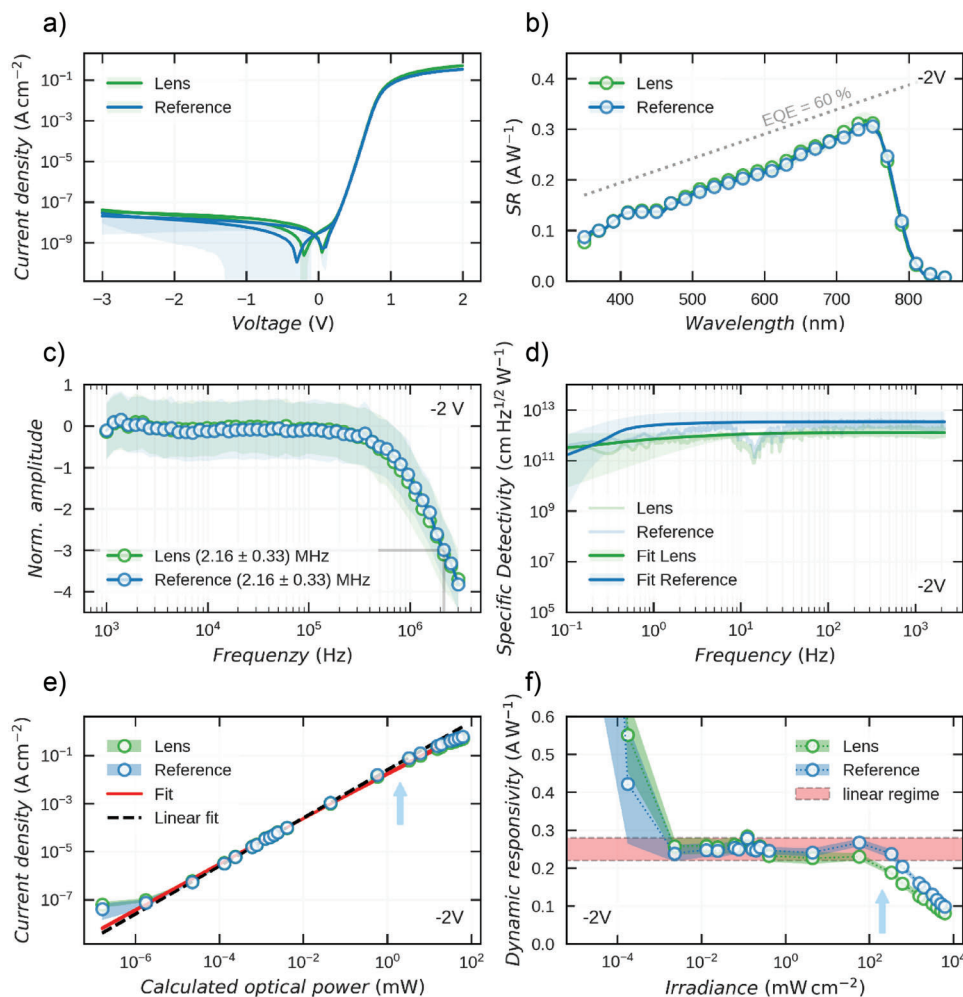


Figure 2. Figures of Merit of the OPDs for 9 reference and 5 lens devices including 1σ standard variations (shaded area): a) Current–voltage characteristic devices in the dark. b) Spectral responsivity devices for different wavelength at -2 V reverse bias. The gray dotted line represents a spectral responsivity equivalent to an EQE = 60%. c) Electrical bandwidth of the devices measured at -2 V reverse bias. d) Specific detectivity D^* of the devices at -2 V reverse bias. The data shown was calculated from the aggregated noise measurement and the spectral response at 750 nm as described previously.^[4] e) Dynamic range and calculated linear dynamic range (deviation from slope = 1 smaller 5%) at -2 V reverse bias. The red line represents an empirical fit $f = a \log_{10}(bx)x$ that is used in the Supporting Information for the calculation of the FIP for different illumination intensities. f) Calculated dynamic responsivity at -2 V reverse bias as visualization of the nonlinear operation regime of the FIP effect. The red area indicates an extended 1σ standard deviation in which the dynamic responsivity does not change with the irradiance (linear regime).

Supporting Information). We want to highlight the difference in nonlinearity depending on the reverse bias, as can be seen in Figure S5 and S6 (Supporting Information) since it explains the difference in the strength of the FIP effect for different bias as we discuss later.

We observed that the FOM of the devices with microlenses statistically do not differ from the reference devices. This shows that the introduction of microlenses in the device architecture does not disrupt the device functionality. However, we should note that most of the measurements were conducted within the linear regime of the OPDs. Furthermore, as seen in Figure 3a, the area covered by the microlenses compared to the size of the active layer was too small for the FIP to become the dominant effect in the nonlinear regime of the dynamic range measurements. Since we wanted to exploit the FIP effect for proximity measurements, we additionally printed an Ag shadow-mask between the

microlenses. The shadow mask ensures that the incident light only passes through the lens optical path.

In Figure 3a, a microscope picture of the printed microlenses on top of an OPD is shown. The image shows how nine microlenses fit into the 1 mm^2 pixel area defined by the OPD's electrodes. A higher density of microlenses increased the possibility of defects or merging between the adjacent droplets. An image of the lens array with the additional Ag shadow mask can be seen in Figure 3b. As a light source, we used a fiber-coupled LED ($\lambda_{\text{LED}} = 530\text{ nm}$) with a core-diameter of $200\ \mu\text{m}$ and a numerical aperture (NA) of 0.50. Proximity measurements were executed with a motorized linear stage that moves the light source away from the sample (see Figure 3c). The normalized distance dependent photoresponse of the devices with and without lens averaged over three and nine devices, respectively, is plotted in Figure 3d. It can be observed that in both cases the current decreases after a

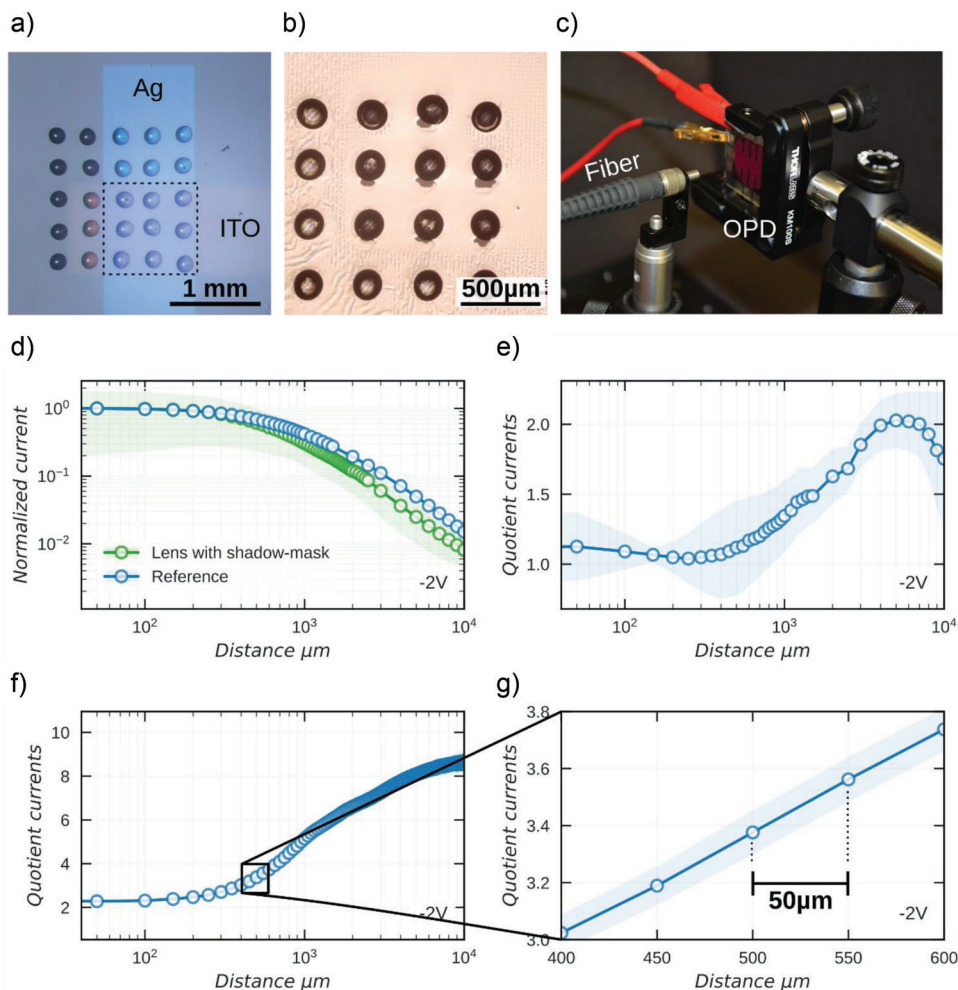


Figure 3. Proximity measurements based on FIP effect: a) Microlens printed via inkjet-printing on the back side of the glass substrate. The pixel is indicated by a dotted square, confined by the Ag and ITO electrodes (scale bar = 1 mm). b) Microlens surrounded and partly covered by a printed Ag shadow mask to make the FIP the dominant response (scale bar = 500 μm). c) Reference device (OPD) and fiber-coupled LED light source on the xyz-stage. d) Light-source distance dependent current normalized to its maximum for 3 lens and 9 reference devices including 1σ standard variations (shaded area). e) Calculated FIP proximity measurements: Quotient between the normalized measured current of the reference and devices with microlenses feature a unique signature for each absolute LED distance. The shaded area represents a 1σ standard variation. f) Quotient for hero devices. The measurement was repeated ten times and averaged. g) Zoom-in demonstrating an accuracy of down to ±50 μm for ten repetitions. The shaded blue area represents a variation of 3 standard variations (3σ).

distance of 200 μm as a result of the decrease in irradiance from the light source moving away. However, the detector containing the microlenses exhibits a more pronounced drop. For larger distances the light is more strongly focused into a smaller spot forcing the OPD further into its nonlinear regime where the photon to electron conversion rate is lower. This shows the occurrence of the FIP effect in accordance to our simulations as described in Section S2 “Simulation proximity measurements and FIP effect” of the Supporting Information. Figure 3e shows the quotient between the reference and microlens device currents. As described by Pekkola et al.^[33] as well as predicted by our simulations (see Figure S10, Supporting Information) this ratio should yield a distance dependent unique signature and can be used for measuring absolute distance. In our devices, the quotient increases steadily distances between 200 μm and 5 mm. For distances < 200 μm, the obtained average ratio is close to one since the normalized

currents are very close to each other. For long distances, the light intensity received by the microlens samples decreases so much that they are driven back into the linear regime. Due to statistic variations in printing the Ag-mask and lens, the relative standard variation of the calculated signature is between 15% and 40%.

To reinforce the significance of the obtained results, we compared proximity measurements conducted at 0 and −2 V reverse bias (Figure S12, Supporting Information). For the samples measured at 0 V, we observed a stronger pronounced drop of the distance dependent photocurrent compared to its counterpart at −2 V reverse bias. We attribute this to the fact that at 0 V the devices with microlens are operated further in their nonlinear regime as can be seen in Figure 2e. Moreover, the photocurrent quotient at 0 V shows a smaller relative standard variation of 5–20% (see Figure S13e, Supporting Information). We related this as well to the operation further in the nonlinear regime, since

hereby the ratio between the device with microlens and the reference becomes larger.

Furthermore, we compared samples with no Ag-shadow mask or an Ag-shadow mask with larger voids to the results obtained with the final mask (see Figure S11 for the different masks, Supporting Information). Samples without shadow mask show no statistically significant difference between responses of the devices with microlens and reference devices (see Figures S12a,b and S13a,b, Supporting Information). Samples with shadow mask with larger voids in comparison to our final mask show a trend indicating the FIP effect (see Figure S13c,d). This trend becomes statistically more accurate for our final Ag-shadow mask that ensures that incident light only passes through the lens optical path (see Figure S13e,f). This shows the relevance of a closed shadow mask for our approach.

In Figure 3f, we showcase proximity measurements for our hero devices with a small step-size of 50 μm measured in the range of 50 μm –10 mm. To gain insight about the maximal achievable resolutions, we average over ten consecutive measurements and examine the standard variation. In Figure 3g, a zoom-in to the short-distance range is shown. A precision of down to $\pm 50 \mu\text{m}$ within three standard deviations (3σ) could be reached by comparing subsequent points and their uncertainties. Moreover, we examining the boundary points of the measurement in order to investigate the measuring range that can be unambiguously used for absolute distance measurements. For a range from 100 μm to 4 mm neighboring points (low distances) or a subselection of points (far distances with reduced resolution) can be distinguished within three standard deviations (3σ) and thus used for absolute distance measuring. For a better view, we present a zoom-in into the data in Figure S14 (Supporting Information). This shows the high potential of the microlens-OPD combination for highly accurate and close-distance proximity applications (see Table 1).

3. Conclusion

The presented work uses inkjet printing technology to fully customize printed microlenses on top of OPDs for close-proximity measurements. We make use of the inkjet technology's freedom of design not only in the xy-deposition by printing the microlenses directly on the pixel but also introduce a process to freely tune their focal length in the z-direction from 150 to 350 μm by printing multiple drops. By using an epoxy-based photoresist surface-layer we further increase the focal length to 775.4 μm . High performance OPDs were investigated in regard of their FOM and in the context of the FIP effect. Low dark current densities j_{Dark} of $20 \pm 10 \text{ nA cm}^{-2}$, high spectral responsivities SR of $310 \pm 20 \text{ mA W}^{-1}$, white noise above $\approx 100 \text{ Hz}$ and specific detectivities D^* of $(1.2 \pm 0.5) \times 10^{12}$ Jones were achieved. We presented relevant proof of the FIP effect and measured distance dependent currents in the range of 50 μm to 10 mm. Hero devices yielded an accuracy of down to $\pm 50 \mu\text{m}$ and the range for absolute distance sensing of 100 μm to 4 mm within three standard deviations (3σ) highlighting the potential of the microlens-OPD combination for highly accurate and close-distance proximity applications. Future work can build on these results and monolithically integrate the reference and lens devices in a streamlined process as well as improve the ratio

between shadow mask and microlens and fully print on flexible or stretchable substrates.

4. Experimental Section

SU-8 Surface Layer: 25 \times 25 mm² ITO-glass substrates were first cleaned in an ultrasonic bath with acetone for 10 min, and then again with isopropanol for 10 min. The substrates were subsequently dried with nitrogen and then treated with oxygen plasma (PlasmaFlecto 30, Plasma technology) for 3 min. A transparent SU-8 layer was deposited on the back of the substrates by spin coating to achieve the desired initial drop contact angle for the lens printing. SU-8 2005 (Microresist) was used in two steps of spin coating: 500 rpm for 10 s and 3000 rpm for 30 s. Subsequently, a prebaking process was carried out on a hotplate at 95 $^{\circ}\text{C}$ for 3 min. Then the samples were UV treated for 3 min, and baked again at 95 $^{\circ}\text{C}$ for 3 min. In order to tune the geometries of the printed microlens, the SU-8 thin film was treated by oxygen plasma for up to 40 s prior to inkjet printing.

Microlens Printing: The SU-8 ink used for microlens consists of 25 wt% SU-8 2150 (Kayaku Advanced Materials) and 75 wt% Erisys GE-20 (Huntsman) as reported in the previous work.^[19] The ink was filtered using PTFE filters with a pore size of 0.2 μm before printing. The inkjet printing process was carried out using the printer PixDro LP50 equipped with a 10 pL cartridge (DMC Fujifilm Dimatix). The temperature of the print head was kept at 35 $^{\circ}\text{C}$, and the substrate temperature was kept at 24 $^{\circ}\text{C}$. After printing, the samples exposed under UV for 3 min. And the samples were baked at 95 $^{\circ}\text{C}$ on a hotplate for 3 min.

Microlenses Characterization and Zemax Simulation: The height of the microlenses were measured by 3D optical profilometer (ContourGT-X, Bruker), the diameter was measured by a light microscope (Axioplan 2 imaging, Carl Zeiss), and the contact angle by a contact angle measuring system (OCA 50, DataPhysics Instruments). The wavelength of light source was set at 550 nm. The refractive index of the microlens material is 1.53 at 550 nm known from preview publication.^[19] In Zemax simulations, the model consists of an object point (diameter: 0), a plano-convex spherical microlens with the convex surface facing toward the object, a glass substrate with the thickness of 1.1 mm and a refractive index of 1.52, and an ITO coating on the other side of the glass substrate with a thickness of 100 nm and a refractive index of 1.92. The entrance pupil was set at the convex surface of the microlens and the value was the same as the diameter of the microlens.

OPD Fabrication: After first printing the lens on the SU-8 thin film on the backside of the pre-structured indium tin oxide (ITO) substrates, OPDs were fabricated via spin coating.

SnO_x nanoparticle ink (Avantama N-31) was filtered with a PVDV filter (0.45 μm pore size) and spin coated with 2000 rpm for 30 s. The layer was annealed 5 min at 120 $^{\circ}\text{C}$ on a hotplate at that was covered with a polyimide foil to protect the microlens. Regioregular poly(3-hexylthiophene-2,5-diyl) (P3HT) and the nonfullerene acceptor IDTBR were mixed 40 g L⁻¹ in 1,2-Dichlorobenzene (CAS: 95-50-1) in a N₂ filled glovebox and stirred overnight. Thereafter they were mixed in a volume ration of 1:1 and after stirring one more hour, filtered at 95 $^{\circ}\text{C}$ with a PTFE filter (0.45 μm pore size) in the glovebox. The active P3HT:IDTBR layer was spin coated in air with (800+300) rpm for (30+20) s, respectively. To dry the still wet layer, devices were vacuum-dried for 60 s. The samples were annealed in the glovebox for 10 min. at 140 $^{\circ}\text{C}$. 30 nm MoO₃ was evaporated as a thermally electron blocking layer and 100 nm silver was evaporated as an electrode. The final pixel size of 1 mm² the OPD is confined by the overlap of the ITO and Ag electrodes. Completed devices were encapsulated with a glass slide and a UV adhesive (Delo-katiobond LP686).

Inkjet-Printed Ag Shadow-Mask: The inkjet printing of the Ag shadow mask was carried out using the printer PixDro LP50 equipped with a 2.4 pL cartridge (DMC Samba Dimatix). Encapsulated devices were placed upside down in a laser cut holder in order to guarantee a planar orientation of the surface. Five seconds of Argon plasma was used to achieve suitable wetting of the printed 30–35 wt% Ag nanoparticle ink (Sigma-Aldrich TGME Silver Dispersion). To align the shadow mask, the microlens with the automated alignment procedure of PixDro was used. The temperature

of the print head was kept at 25 °C, and the substrate temperature was kept at 23 °C. To avoid a change of device morphology by temperature, the printed Ag films were vacuum dried.

OPD Characterization: OPDs were characterized like in the previous works^[7,9,11,44] on OPDs.

Steady-State Characterization: Current–voltage (I – V) characteristics in dark were measured from -3 to 2 V with a source meter unit (Keithley 2636A).

The dynamic range and LDR was measured by changing the intensity of a 500 mW laser (PGL FS-VH) by means of neutral density (ND) filters (Thorlabs NDUVxxA). The calibration of the optical power was performed with a Newport 818-UV photodiode.

Spectral responsivities (SR) were measured with a Xenon-discharge lamp (LOT Arc lamp, 450 W Osram XBO), filtered to the desired wavelengths by a monochromator (Acton, SP-2150i). The light was modulated with a chopper-wheel at 173 Hz and the periodic response of the OPDs were recorded with a lock-in amplifier (SR830, Stanford Research Systems) after amplification with a trans-impedance amplifier (FEMTO DLPCA-200). The system was calibrated with a silicon photodiode (Thorlabs, FDS100).

Noise Spectral Density and Specific Detectivity: The noise spectral density (S_n) was measured by recording the dark current over a period of ≈ 20 s with a nplc = 0.01, yielding 90 000 samples. To avoid the incoupling of pickup-noise, the measurement was conducted in a custom-made shielded box and the signal was amplified with a trans-impedance amplifier (TIA, FEMTO DLPCA-200) directly connected to the box. The output was measured with a source meter unit (Keithley 2636A) and later multiplied with the Hann window function and transformed via a nonuniform discrete Fourier Transform into reciprocal space. Moreover, an isolated low noise voltage source (SIM928, SRS) was used to apply different bias voltages via a BNC connection. The measured SR at 560 nm, the measured frequency-dependent S_n as well as the area A of the OPD were used to calculate the specific detectivity as described in the Review.^[4]

Dynamic Characterization: The speed of the OPDs (-3 dB cut-off frequency) was measured with a periodic optical signal from an Oxxius LBX520 diode laser which was modulated by a square waveform using a function generator (Agilent 33522A). The OPD signal was amplified (TIA, Femto DHPCA-100) and recorded with an oscilloscope (Agilent DSO 6102A).

Proximity Measurements: A fiber-coupled LED ($\lambda_{LED} = 530$ nm, multi-mode fiber) with core-diameter of 200 μ m and a numerical aperture (NA) of 0.50 to approximate a point-like light-source (see Figure 3b) was used. The total optical power was measured with a Newport 818-UV photodiode. The distance dependent power was calculated approximating linear optics and a homogeneous power distribution in the center of the light cone (see the Supporting Information). The intensity of the light was controlled by setting 3 V DC or V_{pp} for modulated 173 Hz square-signals. The current response of the devices was measured with a source meter unit (Keithley 2636A) or a lock-in amplifier (SR830, Stanford Research Systems). In order to increase precision, the starting distance of the linear stage with a fixed metal plate was calibrated. The devices were mounted in a fix sample holder and the yz -positioning of the LED (fiber) was performed by maximizing the measurement current. The resolution of the linear stage is < 0.5 μ m.

Statistical Analysis: Data were used as measured by the instruments. Only in the case of noise measurements a window function is applied to account for errors of the Discrete Fourier transform calculation.

Where applicable data are presented as lines with a shaded area to represent the mean $\pm 1\sigma$ standard deviation or in case of the hero devices the mean $\pm 3\sigma$ standard deviation. For Figure 2, the total number of reference devices was 9 and an additional 5 devices deploy integrated microlenses.

In Figure 3a,b, a total of 9 Devices are used for the reference and 3 devices for the lens covered with the appropriate Ag shadow mask. Two devices with microlenses were destroyed during the experiments due to a crash into the light source and due to false coverage with Ag by printing the shadow mask. For the hero devices, one reference and one lens device are combined to plot the quotient. Each of them were measured ten times in a row to test reproducibility. To compare for the resolution and range

of the hero devices neighboring points were determined to be significantly different when they had no overlap of their $\pm 3\sigma$ standard deviation.

A custom python module for the experimental evaluation was programmed utilizing standard python libraries of the field like numpy, pandas, matplotlib, and astropy. It has been released under the free software license GPLv3 and can be found under.^[45]

Supporting Information

Supporting Information is available from the Wiley Online Library or from the author.

Acknowledgements

This work was partially funded by the KIT Centers pilot project SoftNeuRo. The authors also gratefully acknowledge the Deutsche Forschungsgemeinschaft (DFG, German Research Foundation) under Germany's Strategy via the Excellence Cluster 3D Matter Made to Order (3DMM2O, EXC-2082/1-390761711) for financial support. A.V.T. thanks the Alexander von Humboldt Foundation for financial support. K.X. thanks the Carl Zeiss Foundation for the financial support. M.S. is grateful for the financial support and mentoring from the German Academic Scholarship Foundation. The authors thank M. Pietsch for fruitful discussions.

Open Access funding enabled and organized by Projekt DEAL.

Conflict of Interest

The authors declare no conflict of interest.

Data Availability Statement

The data that support the findings of this study are available from the corresponding author upon reasonable request.

Keywords

focused induced photoresponse, microlenses, organic photodiodes, printed optics, proximity sensing

Received: January 9, 2023

Revised: February 23, 2023

Published online:

- [1] I. Yun, *Photodiodes – From Fundamentals to Applications*, InTech, London 2012, <https://doi.org/10.5772/3406>.
- [2] B. Nabet, *Photodetectors: Materials, Devices and Applications*, Elsevier, Amsterdam 2016.
- [3] S. Donati, *Meas. Sci. Technol.* 2001, 12, 653.
- [4] N. Strobel, M. Seiberlich, R. Eckstein, U. Lemmer, G. H. Sosa, *Flex. Print. Electron.* 2019, 4, 043001.
- [5] T. Yokota, P. Zalar, M. Kaltenbrunner, H. Jinno, N. Matsuhisa, H. Kitanosako, Y. Tachibana, W. Yukita, M. Koizumi, T. Someya, *Sci. Adv.* 2016, 2, e1501856.
- [6] Y. Khan, D. Han, A. Pierre, J. Ting, X. Wang, C. M. Lochner, G. Bovo, N. Yaacobi-Gross, C. Newsome, R. Wilson, A. C. Arias, *Proc. Natl. Acad. Sci. USA* 2018, 115, E11015.
- [7] N. Strobel, N. Droseros, W. Köntges, M. Seiberlich, M. Pietsch, S. Schliske, F. Lindheimer, R. R. Schröder, U. Lemmer, M. Pfannmöller, N. Banerji, G. Hernandez-Sosa, *Adv. Mater.* 2020, 32, 1908258.

- [8] G. Dell'Erba, A. Perinot, A. Grimoldi, D. Natali, M. Caironi, *Semicond. Sci. Technol.* **2015**, *30*, 104005.
- [9] N. Strobel, M. Seiberlich, T. Rödlmeier, U. Lemmer, G. Hernandez-Sosa, *ACS Appl. Mater. Interfaces* **2018**, *10*, 42733.
- [10] N. Gasparini, A. Gregori, M. Salvador, M. Biele, A. Wadsworth, S. Tedde, D. Baran, I. McCulloch, C. J. Brabec, *Adv. Mater. Technol.* **2018**, *3*, 1800104.
- [11] M. Seiberlich, N. Strobel, L. A. Ruiz-Preciado, M. Ruscello, U. Lemmer, G. Hernandez-Sosa, *Adv. Electron. Mater.* **2021**, *7*, 2000811.
- [12] Y. Li, H. Chen, J. Zhang, *Nanomaterials* **2021**, *11*, 1404.
- [13] Z. Tang, Z. Ma, A. Sánchez-Díaz, S. Ullbrich, Y. Liu, B. Siegmund, A. Mischok, K. Leo, M. Campoy-Quiles, W. Li, K. Vandewal, *Adv. Mater.* **2017**, *29*, 1702184.
- [14] I. Deckman, P. B. Lechêne, A. Pierre, A. C. Arias, *Org. Electron.* **2018**, *56*, 139.
- [15] A. Perevedentsev, H. Mejri, L. A. Ruiz-Preciado, T. Marszalek, U. Lemmer, P. W. M. Blom, G. Hernandez-Sosa, *Adv. Opt. Mater.* **2022**, *10*, 2102397.
- [16] Y. Wang, J. Kublitski, S. Xing, F. Dollinger, D. Spoltore, J. Benduhn, K. Leo, *Mater. Horiz.* **2022**, *9*, 220.
- [17] N. Strobel, R. Eckstein, J. Lehr, U. Lemmer, G. Hernandez-Sosa, *Adv. Electron. Mater.* **2018**, *4*, 1700345.
- [18] N. Jürgensen, B. Fritz, A. Mertens, J.-N. Tisserant, M. Kolle, G. Gormard, G. Hernandez-Sosa, *Adv. Mater. Technol.* **2021**, *6*, 1900933.
- [19] Q. Zhang, M. Schambach, S. Schliske, Q. Jin, A. Mertens, C. Rainer, G. Hernandez-Sosa, M. Heizmann, U. Lemmer, *Adv. Opt. Mater.* **2022**, *10*, 2200677.
- [20] L. Jacot-Descombes, M. R. Gullo, V. J. Cadarso, J. Brugger, *J. Microelectromech. Microeng.* **2012**, *22*, 074012.
- [21] D. Xie, H. Zhang, X. Shu, J. Xiao, *Opt. Express* **2012**, *20*, 15186.
- [22] R. Magazine, B. van Bochove, S. Borandeh, J. Seppälä, *Addit. Manuf.* **2022**, *50*, 102534.
- [23] M. Blattmann, M. Ocker, H. Zappe, A. Seifert, *Opt Express* **2015**, *23*, 24525.
- [24] Y. Zhao, Q. Li, J.-B. Doucet, P.-F. Calmon, F. Mesnilgrente, B. Reig, C. Tronche, T. Camps, J. Perchoux, V. Bardinal, *Appl. Sci.* **2019**, *9*, 5484.
- [25] D. J. Hayes, T. Chen, *Proc. SPIE* **2004**, *5435*, 83.
- [26] C.-H. Tien, C.-H. Hung, T.-H. Yu, *J. Disp. Technol.* **2009**, *5*, 147.
- [27] E. J. Markvicka, J. M. Rogers, C. Majidi, in *2020 IEEE/RSJ International Conference on Intelligent Robots and Systems (IROS)*, IEEE, Piscataway, NJ **2020**, pp. 8882–8888.
- [28] E.-C. Chen, C.-Y. Shih, M.-Z. Dai, H.-C. Yeh, Y.-C. Chao, H.-F. Meng, H.-W. Zan, W.-R. Liu, Y.-C. Chiu, Y.-T. Yeh, C.-J. Sun, S.-F. Horng, C.-S. Hsu, *IEEE Trans. Electron Devices* **2011**, *58*, 1215.
- [29] *Datasheet VCNL4010 Fully Integrated Proximity and Ambient Light Sensor With Infrared Emitter, I²C Interface, and Interrupt Function*, <https://www.vishay.com/docs/83462/vcni4010.pdf> (accessed: December 2022.) **2018**.
- [30] C.-H. Chen, C.-F. Lin, K.-H. Wang, H.-C. Liu, H.-W. Zan, H.-F. Meng, W. Hortschitz, H. Steiner, A. Kainz, T. Sauter, *Org. Electron.* **2017**, *49*, 305.
- [31] J.-S. Liao, K.-H. Wang, H.-W. Zan, H.-F. Meng, P.-H. Yeh, C.-C. Tsai, W. Hortschitz, H. Steiner, T. Sauter, in *2016 IEEE International Instrumentation and Measurement Technology Conference Proceedings*, IEEE, Piscataway, NJ **2016**, pp. 1–6.
- [32] T. Oka, H. Nakajima, M. Tsugai, U. Hollenbach, U. Wallrabe, J. Mohr, *Sens. Actuators, A* **2003**, *102*, 261.
- [33] O. Pekkola, C. Lungenschmied, P. Fejes, A. Handreck, W. Hermes, S. Irle, C. Lennartz, C. Schildknecht, P. Schillen, P. Schindler, R. Send, S. Valouch, E. Thiel, I. Bruder, *Sci. Rep.* **2018**, *8*, 9208.
- [34] A. Bablich, M. Müller, P. Kienitz, R. Bornemann, C. O. Ogolla, B. Butz, B. Choubey, P. H. Bolívar, *Sci. Rep.* **2022**, *12*, 10178.
- [35] Y. Wang, J. Benduhn, L. Baisinger, C. Lungenschmied, K. Leo, D. Spoltore, *ACS Appl. Mater. Interfaces* **2021**, *13*, 23239.
- [36] E. Kasparavicius, S. Nakamichi, M. Daskeviciene, M. Marcinkas, L. M. Svirskaitė, C. Lungenschmied, T. Malinauskas, V. Getautis, I. Bruder, *J. Electron. Mater.* **2019**, *48*, 5843.
- [37] P. Krebsbach, S. Schliske, N. Strobel, M. Seiberlich, L. A. Ruiz-Preciado, C. Rainer, X. Huang, U. Lemmer, G. Hernandez-Sosa, *ACS Appl. Electron. Mater.* **2021**, *3*, 4959.
- [38] C. G. Shuttle, R. Hamilton, B. C. O'Regan, J. Nelson, J. R. Durrant, *Proc. Natl. Acad. Sci. USA* **2010**, *107*, 16448.
- [39] S. R. Cowan, J. Wang, J. Yi, Y.-J. Lee, D. C. Olson, J. W. P. Hsu, *J. Appl. Phys.* **2013**, *113*, 154504.
- [40] C. Labanti, J. Wu, J. Shin, S. Limbu, S. Yun, F. Fang, S. Y. Park, C.-J. Heo, Y. Lim, T. Choi, H.-J. Kim, H. Hong, B. Choi, K.-B. Park, J. R. Durrant, J.-S. Kim, *Nat. Commun.* **2022**, *13*, 3745.
- [41] L. J. A. Koster, V. D. Mihailetschi, H. Xie, P. W. M. Blom, *Appl. Phys. Lett.* **2005**, *87*, 203502.
- [42] L. J. A. Koster, M. Kemerink, M. M. Wienk, K. Maturová, R. A. J. Janssen, *Adv. Mater.* **2011**, *23*, 1670.
- [43] J. Hong, C. Yang, X.-H. Li, Y.-H. Chong, H.-D. Xu, *Microwave Opt. Technol. Lett.* **2011**, *53*, 2325.
- [44] N. Strobel, *Printed Organic Photodiodes with Enhanced Performance and Simplified Processing*, Karlsruhe Institute of Technology (KIT), Karlsruhe **2020**, <https://doi.org/10.5445/IR/1000119180>.
- [45] M. Seiberlich, G. Hernandez Sosa, **2023**, <https://doi.org/10.5445/IR/1000156174>. (accessed: January 2023.)